Geophys. J. Int. (2004) **156,** 595-614

A one–way wave equation for modelling seismic waveform variations due to elastic anisotropy

D.A. Angus, C.J. Thomson & R.G. Pratt

Department of Geological Sciences and Geological Engineering, Queen's University, Kingston, ON, Canada K7L 3N6

Submitted to GJI: November 2002

SUMMARY

A new one–way wave equation for three–dimensional anisotropic elastic media and its finite–difference implementation are described. Backscattering is neglected, but the method should provide a sufficiently accurate, efficient (slower than ray theory, faster than full wave equation finite differences) and robust simulation of the primary wave(s) passing through a region of variable and possibly–strong anisotropy. In particular, frequency–dependent wavetype coupling and the effects of rapidly–rotating polarization eigenvectors will be included. Example waveforms are presented for rock elasticities representative of mantle, crustal and basin–scale applications. These have been computed only for homogeneous regions, which facilitates comparison with a separation–of–variables reference solution. Nevertheless, seemingly characteristic waveform effects associated with conical points, or acoustic axes, are observed and these effects should only be modified in degree rather than style by smooth parameter gradients (e.g. in the upper mantle). These characteristics include: merging/splitting pulses, sometimes resulting in simple pulse broadening; wavefront 'tearing'; gaps/lacunae/polarity–reversals in the 'anomalous' component arising from the eigen–polarization rotation; and incipient Hilbert–transform like first–motion changes due to indentations of the slow shear–wave slowness sheet.

Key words: body waves, anisotropy, one–way wave equation, finite–differences, mode coupling, seismic waveforms.

1 INTRODUCTION

Although the presence in the Earth of significant fine–scale (e.g. crystalline) elastic anisotropy is widely acknowledged, orientation variations and averaging make its net effect on longer–scale (or wavelength) seismic signals difficult to assess. Statistical isotropy has generally been a workable hypothesis, though a common extension is to model structures associated with a single axis of alignment, such as parallel cracks, as hexagonally symmetric or transversely isotropic (TI). Having two orthogonal alignments leads to models based on orthorhombic symmetry. Extended approximations such as these hold out the promise of invertible relationships between seismic observables, such as the moveout of exploration–seismic reflections, and the enlarged set of elastic parameters (Bakulin et al., 2000). Sometimes the observables themselves are few in number, such as the two splitting parameters of teleseismic SKS, but still they provide useful insights into the Earth (e.g. Helffrich et al., 2002).

Rocks only approximate to the simple symmetries mentioned and on the single–crystal scale anisotropy can be very strong as well as asymmetric. Direct evidence for the variety of whole–rock elasticities comes from hand–sample measurements (e.g. Mainprice & Silver, 1993; Weiss et al., 1999; Lloyd & Kendall, 2003), although for scales much less than a seismic wavelength. Three–dimensional variations in degree and type of anisotropy must exist on somewhat larger scales controlled by processes such as convection in the mantle, crustal shear–zone tectonics or salt migration. One approach informs us about the possible induced seismic properties by combining lattice preferred orientation (LPO) theory with finite–deformation histories from particular geophysical flow models (e.g. Blackman et al., 1996, for the upper–mantle scale and Raymer et al., 2000, for the sedimentary–basin scale). Observationally, teleseismic evidence for anisotropic layering in an Archean craton (Bostock, 1997) may reveal zones of weakness and high shear indicative of basic craton–formation mechanisms. Variations in lithospheric anisotropy within a craton can also be observed in teleseismic body–wave data (e.g. Kay et al., 1999, for SKS). Combining with complementary signals, such as surface waves or controlled–source arrivals, then provides important contraints on tectonic hypotheses (Kendall et al., 2002). Even on the engineering scale, lithological layering may combine with grain shape as well as crystal orientation to

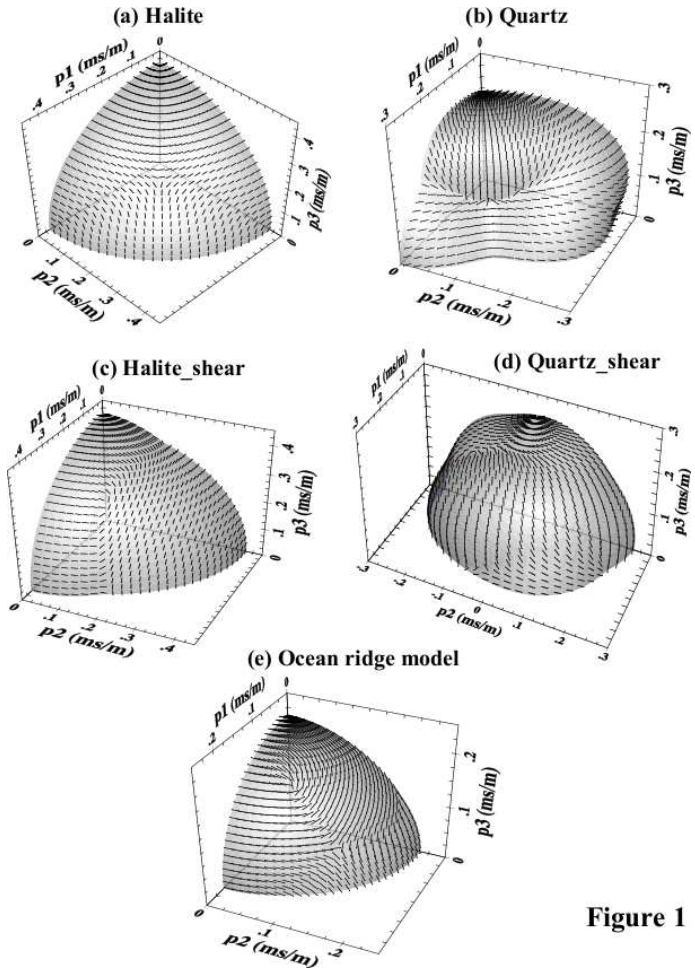

Figure 1

Figure 1. The slow quasi–shear or qS2 wave slowness surfaces for the five sets of anisotropic elastic parameters described in the text. Only a representative portion of each surface is shown. The thin lines embedded in the surfaces indicate the allowed qS2 polarization for a plane wave propagating in the direction corresponding to each line's midpoint. The conical point singularities can be discerned by looking for places where the polarizations form a 'T' pattern. For example, in part (a) Halite such a point lies in the (1,1,1) direction in the natural coordinate system of the figure, which coincides with the line of sight for this 3D perspective plot

produce a net anisotropic fabric in rocks which can augment or overwhelm more–commonly discussed aligned–crack signatures in cross–borehole aquifer imaging (Herwanger et al., 2003; G. Lloyd & S. Valcke, pers. comm.).

These examples indicate the range of complex targets and scales for modern seismic–anisotropy studies. However, the rapid improvements in data quantity and quality due to more complete earthquake networks (e.g. POLARIS in Canada – www.polarisnet.ca) or the burgeoning acquisition for reservoir characterization (e.g. Christie et al., 2002) need to be matched by improved waveform modelling tools based on physically–motivated approximations. Such approximations must relate directly to local material properties and yet describe the frequency–dependent smoothing that takes place during wave propagation.

Interference between the anisotropic quasi–shear (qS) waves is the most diagnostic wave–propagation effect. Sometimes two distinct shear waves are apparent (Winterstein & De, 2001; Guest et al., 1993). If they are not apparent one can infer only that the two shear–wave speeds are close together in the particular propagation direction sampled. There are three types of coalescence, referred to here as 'ring intersections', 'kiss' and 'conical' points (after Crampin & Yedlin, 1981). The first can occur in perfectly TI media, where the two qS sheets of the 'slownes surface' (Musgrave, 1972) and their associated eigen–polarizations can be thought of as passing smoothly through each other on a ring around the symmetry axis. Although the two qS sheets may appear locally simple and analytically independent, in a gradient these waves will nevertheless couple strongly near the ring intersection (Chapman & Shearer, 1989). At a kiss singularity the two qS sheets meet tangentially at an isolated point, as can happen on the axis of TI media. At conical points two slowness sheets meet like two cones tip–to–tip. The point singularities (kiss and conical) define directions in the material which are called 'acoustic axes' by analogy with optical axes used in mineral identification.

The character of polarization–eigenvector rotation is a distinguishing feature for these acoustic axes. Around kiss singularities one qS polarization is radial from the axis and the other is azimuthal about the axis. As a circuit is completed around this type of axis on a given slowness sheet the associated eigen–polarization returns to its original value (Chapman & Shearer, 1989; Figure 12). Conical points are more

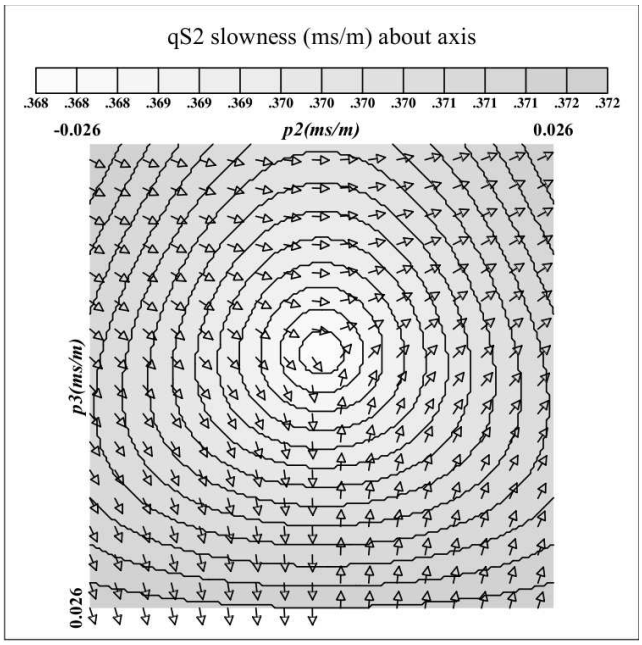

Figure 2

Figure 2. Contours of the (rotated) 1–component of the qS2 slowness in the vicinity of the pure halite acoustic axis. The rotated 1–axis and overall propagation direction are out of the page at the centre of this plot, corresponding to the (1,1,1) direction in the natural coordinates of Figure 1(a). The 'free' polarization eigenvectors have been given arrowheads to emphasize the line of singularity which arises in any scheme which tries to define polarization continuously as the acoustic axis is encircled. In this case the singular line falls straight down from the centre. This singular line not withstanding, the three–fold symmetry about the axis is apparent.

complicated. As a circuit around a conical–point acoustic axis is completed the given eigen–polarization vector reaches the negative of its original value (Rümpker & Thomson, 1994). In actual fact, conical points may be called the most elemental. This is because adding a triclinic perturbation to a TI or hexagonal material causes a ring intersection or kiss singularity to degenerate into multiple conical points (A'lshits & Lothe, 1979) and a slowness–sheet circuit around two conical points will bring the eigen–polarization back to its original value.

Figure 1(a) shows the slow shear wave (qS2) slowness sheet around the (1,1,1) conical–point acoustic axis of cubic halite (elastic parameters taken from Raymer et al. (2000)). The three–fold symmetry is clearly revealed by the characteristic rotation of the eigen–polarization and we see that on opposite sides of the conical point the eigen–polarizations on this sheet are orthogonal (i.e. polarization rotates through $\pi/2$ on travelling half a circuit around the axis). A similar situation exists on the underlying fast quasi–shear (qS1) sheet, except that for each direction in slowness space the eigen–polarizations on the two sheets are orthogonal to each other. From the perspective of Figure 1(a) the strength of halite's anisotropy (i.e. deviation of the slowness surface from a sphere) may not be too apparent, but the singularity of the polarization is as diagnostic as an optical axis for mineralogy. A section through through the qS2 sheet would show that it is sharply indented around the axis and that the conical shape points inwards. The outward normals of the slowness–sheet in this neighbourhood therefore cross each other and this leads to folding of an initially gently–curved wavefront travelling subparallel to the axis, since the normals define the propagation direction of rays and energy flux (i.e. group velocity).

All conical points are the same in a topological sense and Figure 1(b–e) indicates their ubiquity, beginning with another common single–crystal example, quartz (elastic parameters taken from Lloyd & Kendall, 2003, Table 2). The quartz variations are extreme and in fact there are three neighbouring conical points in the severely indented region depicted in Figure 1(b) (this can be seen better in Figure 7 later). Figure 1(c) is the result of numerical LPO calculations for polycrystalline halite (Raymer et al., 2000, Table 1 for the case shear strain 10). Figure 1(d) is the result of laboratory (electron–backscattering) measurements of a whole–rock mylonite sample (Lloyd & Kendall, 2003; for this figure we have used the mylonite sheared–zone–margin elasticity of their Table 3). The last example Figure 1(e) is taken from the numerical study by Blackman et al. (1996) of mid–ocean ridge flow–induced texture in mantle rocks (olivine LPO). We have taken the elastic parameters for their buoyant model at about 30km from the ridge axis and a depth of about 75km (see Figure 4 of Blackman et al., 1996). The 'whole rock' cases (Figure 1(c–e)) are all triclinic.

All these examples are characterized by regions of swirling polarization, focussed on the acoustic axes. The shear–wave splitting (difference between qS1 and qS2 wavespeeds) will be greatest far from the axes, where the polarizations are 'stable'. At the axes the eigen–polarizations are most rapidly changing and hence are potentially diagnostic, but the splitting is least. We should anticipate, then, that the sizeable intermediate or transition directions in 'slowness space' will be of most practical interest.

However, rapid rotation of eigen–polarizations in slowness space does not necessarily imply that a total wavefield displacement vector in physical space will show similar rapid variations as a result of small changes in propagation direction (e.g. across a gently–curved wavefront

propagating along the acoustic axis). Rather, the wave energy will be distributed between the roughly–orthogonal qS1 and qS2 eigen–polarizations such that the net displacement is more–slowly varying. Since their wavespeeds diverge away from axes, a frequency–dependent transition between split and degenerate waveforms is expected and its differing characteristics on the various displacement components are potentially diagnostic, if we can systematize them.

Wave–coupling methods exist for problems such as this. For example, Chapman & Shearer (1989) considered depth–dependent media using separation of variables and described essential properties of the intersection and kiss coupling parameters and resulting waveforms. Rümpker & Thomson (1994) studied the effects of conical points on curved wavefronts in depth–dependent media. Their work included ray tracing, documenting the complete separation of the initial wavefront into two distinct fronts, the folding of the slower front, and very high–frequency waveforms for which the effects of both qS coupling and wavefront folding were considered (using Runge–Kutta 1–D finite differencing and 2–D integration over lateral slowness). Vavryčuk (1999) studied kiss singularities and found the interesting result that standard higher–order ray theory terms are of use in describing the coupling. Most recently, Rümpker & Kendall (2002) combined ray coupling and perturbation theory with the ideas of Maslov slowness integration (or 'Snell wave' summation), to give a rapid computation method valid near folded wavefronts (caustics) without the need to assume lateral homogeneity. These papers and the book by Kravtsov & Orlov (1990), for example, give good introductions to the relevant ray and perturbation–theory literature. Of course, full–wave numerical solutions are also applicable, of which the spectral–element method (Komatitisch & Tromp, 1999) is one which gives most impressive results for the global examples presented by its authors.

An intermediate approach is demonstrated here, one which is in some sense local, is not too computationally intensive and yet is not built explicitly on rays. The presentation in §2 proceeds from first principles and is meant to be self–contained. The problem consists of finding a method which can incorporate a limited spectrum of plane waves, the curvature of their underlying envelope and the eigen–polarization rotations. Readers familiar with the solutions for depth–dependent media (separation of variables and Fourier integration over slowness) will find the derivation has some conventional features and those interested in an alternative, more detailed, derivation may refer to Thomson (1999). Global (in fact Cartesian) coordinates are used, as opposed to coordinates based on the rays in the true medium. The method has the potential to produce finite–frequency waveforms which filter out fine details of the stucture according to the wave equation. In fact, the method is a new wave equation in itself, and the means used to solve it numerically are somewhat secondary.

The basic theory and its implementation are explained in §§2–4. In §5 we study the waveforms predicted for media characterized by the slowness surfaces in Figure 1 and attempt to draw some general conclusions from the modelling.

2 NOTATION AND THE BASIC FACTORIZED WAVE EQUATION

Consider at first a single plane wave in a homogeneous anisotropic medium, characterized by its slowness vector $\mathbf{p}$. The normal to the wave or phase front defines the direction of $\mathbf{p}$ and the magnitude of $\mathbf{p}$ depends on whether the wave is quasi–compressional (qP) or quasi–shear (qS1, qS2). For each wavetype there is a corresponding polarization eigenvector and the three eigenvectors corresponding to a single direction of $\mathbf{p}$ are mutually orthogonal. These basic results can be found in Musgrave (1972) or Červený (2001, Chapter 2).

Let the Cartesian coordinates be $\mathbf{x} = (x_1, x_2, x_3)$ and let the waves propagate subparallel to the x_1 axis. The lateral or cross coordinates can then be denoted x_α, $\alpha = 2, 3$. An alternative description of a plane wave begins by specifying the lateral slowness components p_α. Then the remaining 1–component $P_1(p_\alpha)$ depends on the wave type and can be found from the 'Christoffel' equation (Červený, 2001). We assume the direction of propagation is close to the 1–axis and that all three wave types are propagating (i.e. not evanescent), so that the p_α are small and the three allowed values of P_1 are real. The three polarization eigenvectors in this common lateral slowness description are no longer exactly orthogonal, but they do form a useful basis. Let these eigenvectors form the columns of the (3×3) matrix $\mathbf{G}$, which is invertible since the eigenvectors are not collinear. The corresponding 1–slownesses form the elements of the (3×3) diagonal matrix $\mathbf{P}_1$.

The frequency–domain plane wavefield may be written $\mathbf{u}(x_1, x_\alpha, p_\alpha, \omega)$, and we suppose that it contains in general all three wave types with a common p_α. In a homogeneous medium this combined wavefield obeys the one–way wave equation

$$\partial_1 \mathbf{u} - \mathrm{i}\omega \quad \mathbf{u} = 0\,, \qquad\qquad (p_\alpha) = \mathbf{G}\mathbf{P}_1\mathbf{G}^{-1}\,, \tag{2.1}$$

exactly. The action of the 'propagator' matrix can be visualized as follows. First $\mathbf{G}^{-1}$ decomposes the total plane–wave displacement field into qP, qS1 and qS2 amplitudes. Then the diagonal matrix $\mathrm{i}\omega\mathbf{P}_1$ imparts the appropriate phase shifts for a propagation step along x_1. Lastly $\mathbf{G}$ combines the three evolved wave amplitudes into the new total wavefield.

When the initial field is not a sum of single–slowness plane waves we must use 2–D Fourier plane–wave decomposition, given by the transforms

$$u(p_\alpha) = \int u(x_\alpha) \exp[-\mathrm{i}\omega p_\alpha x_\alpha] dx_\alpha\,, \qquad u(x_\alpha) = \left(\frac{\omega}{2\pi}\right)^2 \int u(p_\alpha) \exp[\mathrm{i}\omega p_\alpha x_\alpha] dp_\alpha\,. \tag{2.2}$$

The propagator acts on each p_α or 'Snell wave' component $\mathbf{u}(p_\alpha)$ of the wavefield $\mathbf{u}(x_\alpha)$ and the one–way equation now becomes

$$\partial_1 \mathbf{u} = \left(\frac{\omega}{2\pi}\right)^2 \int\int \mathrm{i}\omega \quad (x_\alpha, p_\alpha) \exp[\mathrm{i}\omega(x_\alpha - y_\alpha)p_\alpha]\mathbf{u}(y_\alpha) dy_\alpha dp_\alpha\,. \tag{2.3}$$

Reading from the right, the wavefield data are initially specified on the plane $x_1 = constant$, with y_α as the lateral–position dummy variable.

These data are Fourier transformed from y_α to the lateral–slowness p_α domain. For each p_α or Snell wave, and at each x_α, the corresponding total displacement $\mathbf{u}(p_\alpha)$ is carried forwards by the matrix propagator , which appropriately analyses the three wavetypes as described above. Finally, inverse Fourier transformation w.r.t. p_α combines the Snell waves to yield the total (first derivative of) $\mathbf{u}$ at x_α.

This formula seems intuitively reasonable for a homogeneous medium and the one–way wave equation (2.3) is then in a sense an exact 'factor' of the full anisotropic elastic wave equation (i.e. for the propagating waves at least). In a smooth inhomogeneous medium, though, it can only be approximate. Backscattering from gradients is obviously neglected and in fact this equation is then the first term in an asymptotic expansion in powers of ω^{-1} of the factorized wave equation given by Thomson (1999). The elements of depend in general on x_α as well as p_α, so that lateral variations of the medium come into play at each propagation step via the variations in the local 1-slownesses and eigen–polarizations with x_α. An important and desirable property of the propagator matrix is that its elements are slowly varying even in the vicinity of an acoustic axis, where the individual qS polarizations are singular.

The derivation of (2.3) makes no explicit assumptions about p_α being small, apart from the assumption that the forward slownesses in $\mathbf{P}_1$ are real, and hence this equation is valid for a range of 'wide' angles. However, in practice the assumption that only positive or 'forward' values of the 1–slownesses P_1 are important becomes unrealistic at wide angles. This is especially true if there is anisotropy and dimples on the slowness surface lie close to the x_α directions. In that case the plane–wave group velocity corresponding to p_α may have a positive x_1 component even if the full slowness vector (P_1, p_2, p_3) has a negative 1–component. In practice, therefore, (2.3) is to be used only for a limited range of p_α and further approximations are possible (§3).

The interpretation of the propagator makes it apparent how to isolate or filter out particular wave types. For example, if only qP waves are wanted it may seem natural to use only the qP eigen–polarizations and 1–slownesses when forming . It is also easy to extract a reference phase from the propagation step. Lastly, we mention that by a few more steps and approximations (Thomson, 1999, §5.4) the propagation scheme outlined can be recast as something very close to the phase–screen method (Wu, 1994; Le Rousseau & de Hoop, 2001). This significantly reduces the computational effort in the wide–angle, laterally–varying case. However, we presently take a different approach to simplification.

3 THE REDUCED ONE–WAY WAVE EQUATION

The propagator can be constructed directly without first determining the individual eigen–polarizations and slownesses. Let the elastic parameters be denoted by c_{ijkl} and define the matrix subset $\mathbf{C}_{jk}$ by $(\mathbf{C}_{jk})_{il} = c_{ijkl}$. Then by considering the Christoffel equation defining the individual eigenvectors and slownesses it can be observed that the composite quantity (x_α, p_α) is a solution of the matrix equation (Thomson 1999, §2.1)

$$\mathbf{B} = (\quad + \mathbf{A})^2 + [\mathbf{A}, \quad] \,, \tag{3.1}$$

where

$$\mathbf{A} = \frac{1}{2}\mathbf{C}_{11}^{-1}(\mathbf{C}_{1\alpha} + \mathbf{C}_{\alpha 1})p_\alpha \,, \tag{3.2}$$

$$\begin{aligned} \mathbf{B} &= \mathbf{A}^2 - \mathbf{C}_{11}^{-1}\mathbf{C}_{\alpha\beta}p_\alpha p_\beta + \rho\mathbf{C}_{11}^{-1} \\ &= \frac{1}{4}\mathbf{C}_{11}^{-1}(\mathbf{C}_{1\alpha} + \mathbf{C}_{\alpha 1})\mathbf{C}_{11}^{-1}(\mathbf{C}_{1\beta} + \mathbf{C}_{\beta 1})p_\alpha p_\beta - \mathbf{C}_{11}^{-1}\mathbf{C}_{\alpha\beta}p_\alpha p_\beta + \rho\mathbf{C}_{11}^{-1} \end{aligned} \tag{3.3}$$

and the final 'commutator' term in (3.1) is given by $[\mathbf{X}, \mathbf{Y}] = \mathbf{XY} - \mathbf{YX}$. The x_α (and indeed x_1) dependence of arises from those of the elasticity c_{ijkl} and density ρ.

For narrow angles, as could be appropriate when the incident wave is 'almost plane', we may seek an expansion about $p_\alpha = 0$:

$$(x_\alpha, p_\alpha) = \mathbf{P}_0 + \mathbf{P}_\alpha p_\alpha + \mathbf{P}_{\alpha\beta}p_\alpha p_\beta + \cdots . \tag{3.4}$$

The expansion coefficients $\mathbf{P}_0(x_\alpha)$, etc., are obtained by substituting (3.4) into the defining equation (3.1) and matching powers of p_α. The first few terms are then found to be given by

$$\mathbf{P}_0 = \sqrt{\rho\mathbf{C}_{11}^{-1}}, \tag{3.5}$$

$$\mathbf{P}_0\mathbf{P}_\alpha + \mathbf{P}_\alpha\mathbf{P}_0 = -\mathbf{C}_{11}^{-1}(\mathbf{C}_{1\alpha} + \mathbf{C}_{\alpha 1})\mathbf{P}_0, \tag{3.6}$$

$$\mathbf{P}_0\mathbf{P}_{\alpha\beta} + \mathbf{P}_{\alpha\beta}\mathbf{P}_0 = -\mathbf{C}_{11}^{-1}\mathbf{C}_{\alpha\beta} - \mathbf{C}_{11}^{-1}(\mathbf{C}_{1\alpha} + \mathbf{C}_{\alpha 1})\mathbf{P}_\beta - \mathbf{P}_\alpha\mathbf{P}_\beta. \tag{3.7}$$

Matrix $\mathbf{C}_{11}$ is real and symmetric. In the isotropic case it is diagonal and its elements relate closely to the inverse wavespeeds (Woodhouse 1974). The eigenvalues and eigenvectors of $\mathbf{C}_{11}$ must be known to construct $\mathbf{P}_0$, which is also symmetric. The higher terms (e.g. (3.6)) all require the solution of nine simultaneous equations for the nine elements of each coefficient matrix (e.g. $\mathbf{P}_\alpha$) and ostensibly the inversion of a 9×9 matrix constructed from $\mathbf{P}_0$. An alternative scheme is possible, though, since $\mathbf{P}_0$ is symmetric. Using (3.6) as an example, the difference between this equation and its transpose leads to three equations for the three independent elements of the antisymmetric part of $\mathbf{P}_\alpha$. Then adding (3.6) and its transpose leads to six simultaneous equations for the symmetric part of $\mathbf{P}_\alpha$. The ascending higher terms can

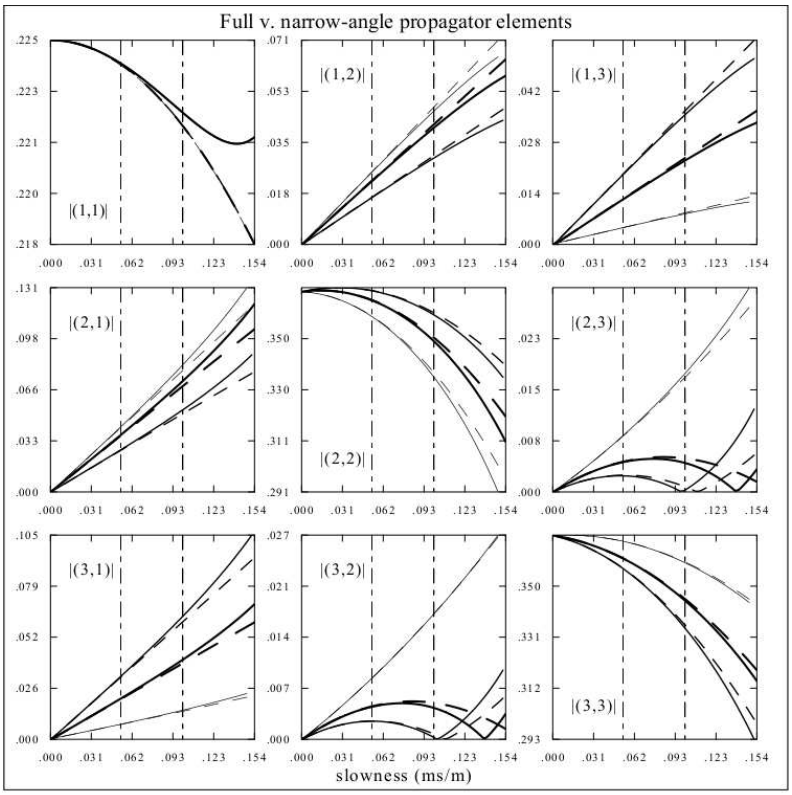

Figure 3

Figure 3. The nine elements of the exact propagator (solid lines) compared to those of the quadratic approximation (3.4) (dashed lines) in pure halite, with expansion point given by the centre of the contour plot in Figure 2 (i.e. the acoustic axis). Only the magnitudes are plotted, as indicated by the labels $|(1,1)|$, etc., for each frame. Each horizontal axis gives the magnitude of the lateral slowness 2–vector (p_2, p_3) or distance from the acoustic axis. Three azimuths have been selected, -10°, 50° and 150°, measured anticlockwise from the p_2–axis. These are signified by the three different lineweights. The two vertical centrelines depict the slownesses corresponding approximately to propagation at 8° and 15° to the 1–direction. At 15° modest differences between the exact and approximate forms can be seen.

all be found by these steps with the various right–hand sides indicated by (3.6) and (3.7). It is systematic and easily coded for a computer, if somewhat tedious.

When the expansion (3.4) is substituted into (2.3) the multiplications by p_α and the inverse Fourier transforms w.r.t. p_α introduce derivatives w.r.t. x_α and factors of $\mathrm{i}\omega$. Truncation after the quadratic term in (3.4) leads to

$$\partial_1 \mathbf{u} = \mathrm{i}\omega \mathbf{P}_0 \mathbf{u} + \mathbf{P}_\gamma \partial_\gamma \mathbf{u} + \frac{1}{\mathrm{i}\omega} \mathbf{P}_{\delta\gamma} \partial_\delta \partial_\gamma \mathbf{u} \tag{3.8}$$

in the frequency domain and

$$\partial_1 \partial_t \mathbf{u} = -\mathbf{P}_0 \partial_t^2 \mathbf{u} + \mathbf{P}_\gamma \partial_\gamma \partial_t \mathbf{u} - \mathbf{P}_{\delta\gamma} \partial_\delta \partial_\gamma \mathbf{u}. \tag{3.9}$$

in the time domain. We term equations (3.8) and (3.9) '15° approximations' by analogy with Claerbout (1976) for acoustic waves, where this name implied that accuracy was deemed acceptable for propagation angles up to about 15° from the x_1 direction. Note that the second/middle term on the rhs does not arise in the acoustic case. In the isotropic elastic case the matrices $\mathbf{P}_\gamma$ have some off–diagonal elements which can be associated with (weak) P to S wave coupling. Perhaps more interestingly, when an anisotropic slowness surface has an asymmetry or 'dip' w.r.t. the x_1 axis (i.e. when that axis is not in a mirror plane) the $\mathbf{P}_\gamma$ matrices will describe its effect on the waves.

Other approximate partial differential equations can be derived from alternative expansions of the propagator (Thomson, 1999), but here we implement only the 15° equation. In practice we suspect that for this vector wavefield problem either the 15° equation will be satisfactory, or we shall adopt a phase–screen approach rather than a higher–order vector partial differential equation derived using, for example, a rational approximation to .

4 FINITE–DIFFERENCE IMPLEMENTATION IN CARTESIAN COORDINATES

The frequency–domain equation (3.8) has been implemented using simple second–order accurate finite differences, where the wavefields at the current and one previous x_1 steps are used to compute the values at the next x_1 step. First, though, we reduce the oscillatory dependence of the wavevector $\mathbf{u}$ on x_1 by extracting a local dominant–phase term according to

$$\mathbf{u} = \exp\left[\mathrm{i}\omega \mathrm{diag}\left(\mathbf{P}_0\right)\left(x_1 - x_1'\right)\right]\bar{\mathbf{u}}\,, \tag{4.1}$$

where $\mathrm{diag}(\mathbf{P}_0)$ is the diagonal part of the matrix $\mathbf{P}_0$, x_1' is taken to be the current x_1 position and the modulation $\bar{\mathbf{u}}$ is expected to be slowly varying about the current x_1. In an isotropic medium $\mathbf{P}_0$ is purely diagonal and in the anisotropic examples to follow the off–diagonal elements are about two orders of magnitude smaller than the diagonals. The off–diagonals in $\mathbf{P}_0$ are, though, generally comparable to the second (dip) and third (curvature/spreading) terms on the rhs of (3.8).

In effect the local wavefield modulation $\bar{\mathbf{u}}$ is stored at $x_1 - \Delta x_1$ and x_1, and a uniform grid spacing Δx_α is used in the lateral directions (at least in the most straightforward case). The lateral derivatives are then represented by the finite–difference formulas

$$\partial_\alpha \bar{\mathbf{u}} = \left(\bar{\mathbf{u}}(x_1, x_\alpha + \Delta x_\alpha, \omega) - \bar{\mathbf{u}}(x_1, x_\alpha - \Delta x_\alpha, \omega)\right)/(2\Delta x_\alpha) + O(\Delta x_\alpha^2)\,, \tag{4.2}$$

$$\partial_\alpha^2 \bar{\mathbf{u}} = \left(\bar{\mathbf{u}}(x_1, x_\alpha + \Delta x_\alpha, \omega) - 2\bar{\mathbf{u}}(x_1, x_\alpha, \omega) + \bar{\mathbf{u}}(x_1, x_\alpha - \Delta x_\alpha, \omega)\right)/(\Delta x_\alpha^2) + O(\Delta x_\alpha^2)\,, \tag{4.3}$$

$$\begin{aligned}\partial_2\partial_3 \bar{\mathbf{u}} = {} & \left(\bar{\mathbf{u}}(x_1, x_2 + \Delta x_2, x_3 + \Delta x_3, \omega) - \bar{\mathbf{u}}(x_1, x_2 + \Delta x_2, x_3 - \Delta x_3, \omega)\right. \\ & \left. -\bar{\mathbf{u}}(x_1, x_2 - \Delta x_2, x_3 + \Delta x_3, \omega) + \bar{\mathbf{u}}(x_1, x_2 - \Delta x_2, x_3 - \Delta x_3, \omega)\right)/(4\Delta x_2 \Delta x_3) \\ & + O(\Delta x_2^2, \Delta x_3^2)\,,\end{aligned} \tag{4.4}$$

and the explicit extrapolation scheme is

$$\bar{\mathbf{u}}(x_1 + \Delta x_1, x_2, x_3, \omega) = \bar{\mathbf{u}}(x_1 - \Delta x_1, x_2, x_3, \omega) + 2\Delta x_1 \partial_1 \bar{\mathbf{u}}(x_1, x_2, x_3, \omega) + O(\Delta x_1^2)\,. \tag{4.5}$$

Although this is a straightforward method which is easily implemented on a standard computer (an Intel/Athlon Processor under Linux in our case), there are some subleties to be considered.

Firstly, one might expect such an explicit finite–difference scheme to be only conditionally stable. In fact, according to Tannehill et al. (1997; p.129 'Richardson's method') a corresponding three–time–level scheme for the scalar heat equation in one space dimension is inherently unstable. There exists a wide range of alternative explicit and implicit finite–difference schemes for heat equations which we could attempt to use here (Tannehill et al. 1997; Chapter 4). However, our numerical results have indicated conditional stability for this simplest of schemes, with a minimum value of the lateral–grid spacing being admissible for a given x_1 step. Sensitivity of the results on the latter has been reduced by the extraction of the local dominant phase and, of course, ours is a (parabolic) wave equation not a heat equation, and a vector one at that. From numerical experience we have found that a useful guideline is given by $\Delta x_1/\omega\Delta x_\alpha <$ 'constant', where 'constant' depends on the elasticity/wavespeed. This simple rule implies that halving the lateral grid spacing may require halving the x_1 step size or doubling the frequency to maintain stability. Although a von Neumann type stability analysis for this matrix equation does not yield a simple analytic stability criterion, we have examined numerically the growth of the matrix equations obtained by substituting a plane–wave ansatz into the finite–difference formulas (D. Angus, Ph.D. thesis), with results that are consistent with the simple rule just quoted.

Accurate finite–difference representation of lateral derivatives, particularly second derivatives, at the perimeter of the lateral grid is more problematic. One–sided second–order difference stencils have been found too inaccurate. We have examined higher–order one–sided schemes (using up to five interior points), but this did not improve matters as Fornberg (1996; Chapter 3) indicates for equi–spaced grids. We also experimented with a variable lateral–grid spacing to refine the mesh near the edges (using the logarithmic method described by Tannehill et al. (1997; p.335) and a Chebyshev scheme as recommended by Fornberg (1996)). However, while this can improve the accuracy of the one–sided finite–difference formulas at the edges, it could do so only by reducing the lateral–grid spacing there by so much that the forward–step size had to be excessively reduced to maintain stability in extrapolation.

The solution to this difficulty was found by noticing that accuracy of lateral derivative representations was only an issue when these were significant, which means when the underlying wavefront is inclined significantly to the x_1 axis. In addition, of course, the higher the frequency the larger the oscillations with respect to x_α and the more difficult it becomes to achieve accuracy. We have circumvented these problems by the following method, which was suggested by preliminary results from a curvilinear–coordinate version of our method (to be presented at a later date). For interior lateral grid points we evaluate the lateral derivatives using the central differences indicated in equations (4.2)–(4.4) above. These are clearly accurate enough for all the frequencies and wavefront curvatures used so far. The x_1 derivatives they lead to via (3.8) at the first two interior grid points near each edge (or corner) point are then used to extrapolate out to that edge point. However, this extrapolation of $\partial_1\mathbf{u}$ is performed only after a lateral–phase term is extracted according to $\partial_1\mathbf{u} = \partial_1\tilde{\mathbf{u}}\exp[\mathrm{i}\omega p_\alpha'(x_\alpha - x_\alpha')]$, where x_α' is the first interior grid coordinate. This extrapolation to the edge has a truncation error of second order in the (uniform) lateral–grid spacing and the only question remaining is how best to choose the local lateral reference slowness p_α'. As a first pass we use the known perimeter lateral slowness of our incident wave, and once this is removed it is possible to iterate by aligning the remaining slightly–different complex phases of the first two interior grid $\partial_1\mathbf{u}$ values. When multiple shear waves are present it may not be obvious what the best lateral slowness should be and this iteration helps. These steps are not overly time consuming.

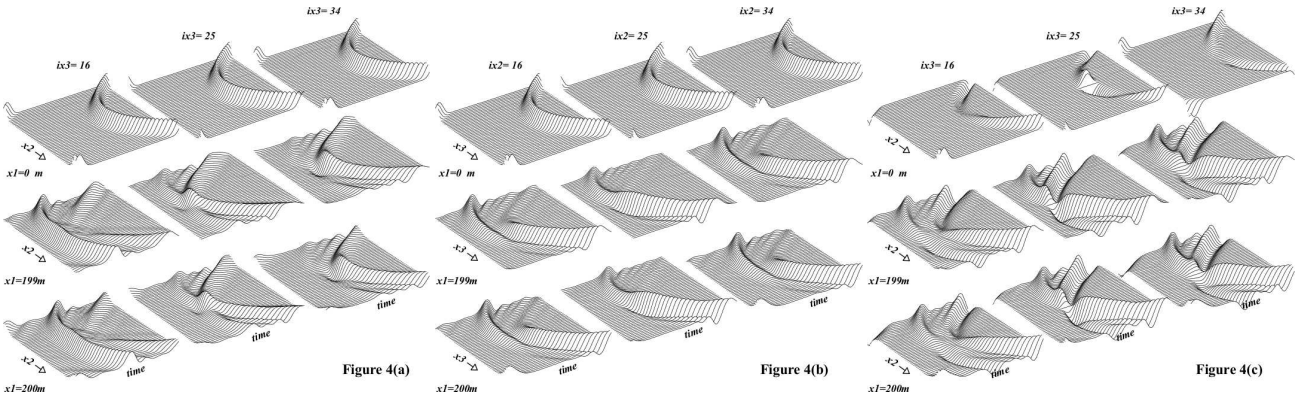

Figure 4. Waveforms of the 2–component at the initial x_1 plane and the last two planes (199m and 200m), plotted as profiles either along the x_2 axis **(a)** or the x_3 axis **(b)**. The indices above the three columns signify the grid position of the profile in the remaining (third) direction. Since the (x_2, x_3) grid has 49×49 points, index 25 represents a precise centre line, while 16 and 34 approximately bisect the intervals on either side. The $x_1 = 0$m frames reveal the curvature of the initial wavefront in comparison with the pulse width. The lower two frame sets indicate the movement of the wavefield in time after a 1m step along x_1. The wrap–around of the discrete time Fourier transform is apparent, but not a concern. Note that the total travel time of the waves is approximately 4 times longer than the plotted time axis (i.e. there is multiple wrap–around and these must be considered reduced–time plots). See text for discussion of the evolved waveforms. Part **(c)** shows the weaker 3–component along x_2 profiles.

A perhaps less–expected complication has been an occasional low–frequency inaccuracy caused by division by ω in (3.8) in combination with imperfect accuracy in the second derivatives. This did not arise for the examples presented here, but we mention it for completeness. Since the one–way equation (3.8) is a high–frequency approximation one should perhaps regard this occurrence as a potentially–useful warning against inappropriate application, rather like end–point signals in slowness integrals.

5 NUMERICAL EXAMPLES

We present waveforms for the five different media in Figure 1, taken to be homogeneous even though this is not required by the theory. Assuming homogeneity facilitates comparison with the reference solution described below, adequately tests the numerical implementation and is sufficient to demonstrate the anisotropic propagation physics currently of most interest. In each case the coordinates are rotated so that the x_1 propagation direction points more–or–less along an acoustic axis. The actual dimensions used in the modelling will be described, though by the end a more scale–independent view of the results will emerge. Essentially the objective is to simulate waves that would be regarded as high frequency for each potential geophysical scenario (upper–mantle turning waves, cross–borehole recording, etc.). This reveals the waveform characteristics most clearly and space limitations necessitate that the qualitative effects of low–pass filtering must generally be surmised.

A smoothly–curved incident wavefront is defined over a square region in the $x_\alpha = (x_2, x_3)$ plane. In most cases the size of this region is 144m$\times$144m and exceptions will be noted as they occur. The wavefront curvature is defined by its normals at the extremes of the 2– and 3–axes and these normals are inclined at angles to x_1 up to about 15°. One can ascertain from the plots below the significance of the wavefront curvature relative to the incident–waveform duration.

The total initial displacement is slowly varying across the incident wavefront and is arbitrarily chosen to be dominantly along x_2. This is achieved by taking at each point on the plane $x_1 = 0$ an appropriate linear combination of the two allowed qS eigen–polarizations corresponding to the wavefront's incidence angle at the point in question. As the individual eigen–polarizations are singular at some point in the plane (because the wavefront directions encompass an acoustic axis), their weights must counter–rotate to form the smooth result.

The incident wavefront carries a simple smoothed delta–function pulse (see Figure 4, top). This pulse has a typical half–width of about 0.3ms (or a width of 0.64ms at its base). A typical propagation path is 200m in the 1–direction and, taking the 1–component of slowness in the pure halite example described first (see Figure 2), this corresponds to roughly (200m)(0.38ms per m)/(0.3ms) $\approx$ 250 spatial pulse half–widths. The waveform effects are certainly extreme after travelling so far.

The waveforms are computed at $nt = 64$ time samples with increment $\Delta t = 0.04$ms and the smooth incident waveform corresponds to a delta function convolved four times with a boxcar of width $4\Delta t$. In practice, sufficiently detailed waveforms have been obtained by extrapolating only the first 17 frequencies (i.e. not all 32 up to the Nyquist). For the longest program runs, the lateral grid of 49×49 points has spacing Δx_α=3m and propagation step $\Delta x_1 = 0.02$m. Thus 10,000 steps are used for a 200m path and this takes approximately 22mins using Gnu fortran77 with a 1.8Ghz Athlon processor running under Linux. An x_1 stepsize 2.5 times larger produces waveforms that are slightly different only at the edges of the domain, where the effects of inaccuracy at the highest frequencies is revealed. At the lower frequencies a larger step size is often permissible and a refinement of the coding would include frequency–variable step sizes.

'Exact' reference waveforms are computed using separation of variables and two–dimensional numerical integration over lateral slownesses p_α. The solution of the exact one–dimensional wave equation in x_1 for each value of the lateral slowness was computed using a

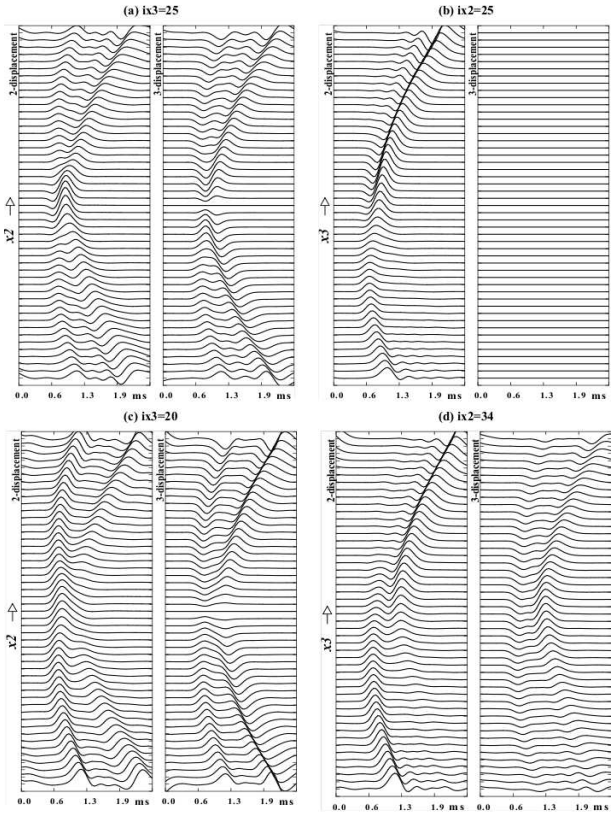

Figure 5

Figure 5. The two lateral components of the displacement in pure halite after 200m of propagation. These plots serve to emphasize that the 3–component has grown from zero to a level sometimes comparable with the original 2–component. **(a)** x_2 section, x_3 midline (ix3=25): Note there is a 'gap' in the 3–component at the central x_2 values. We can expect to see such gaps in general. A precursory negative swing on the 2–component is clearly displayed in the central region. Near the edges there is a hint of some ringing in the waveforms, which may indicate the need for a refined finite–difference mesh, but the quality of the waveforms in the important central region is good. **(b)** x_3 section, x_2 midline (ix2=25): There is no 3–component (by symmetry) and the waveforms of the 2–component are significantly different at large and small x_3. **(c)** x_2 section, x_3 index 20: This shows the apparent enlargement of the 'gap' in the 3–component away from the acoustic axis. **(d)** x_3 section, x_2 index 34: This shows the significance of the 3–component away from the (anti)symmetry plane and the transferance of energy from the fast to the slow qS wave in the 2–component.

layer–matrix program ('Rmatrix', for a single layer in this case) developed by Martin & Thomson (1997), and the numerical slowness integrations were performed using either a simple trapezium rule or the Filon method (Frazer & Gettrust, 1984). The initial conditions were chosen to duplicate those used for the one–way equation. End–point (or, rather, perimeter) effects in the slowness integrals mean a comparison can only be made in the central regions. No attempt has been made to suppress these perimeter effects, which are indicated below where they are apparent.

5.1 Pure Halite – a symmetric example

For cubic pure halite we set the propagation direction x_1 to be along the (1,1,1) acoustic axis in the natural reference frame of Figure 1(a), and x_3 is set to point towards the natural–frame (0,0,1) axis. The 1–component P_1 of the incident wave qS2 slowness in this rotated frame is contoured over (p_2, p_3) in Figure 2, where the singular qS2 polarizations are also shown. The three–fold symmetry about the axis is evident, as is a line of singularity in these 'free' polarization eigenvectors.

The accuracy of the Taylor expansion (3.4) is crucial to the method and Figure 3 shows the exactly–evaluated elements of (2.1) versus those of its quadratic approximation about the point $p_\alpha = 0$ (i.e. the first three terms of (3.4)). Visual inspection indicates that the second–order expansion has reasonable accuracy out to 15°, even though this expansion is effectively about a singular point of the slowness surface. We have experimented by moving the expansion point around in the neighbourhood of the acoustic axis, with stable results. When one recalls that the individual matrix components of are singular, it is gratifying that the Taylor series for the product matrix is indeed so stable. The true acceptability or otherwise of the apparently–accurate quadratic approximation in Figure 3 can only be ascertained by looking at the resultant waveforms, however.

Figure 4 shows the waveform 2–components along profiles parallel to x_2 and x_3, at the initial plane and at $x_1 = 199$m, 200m. The

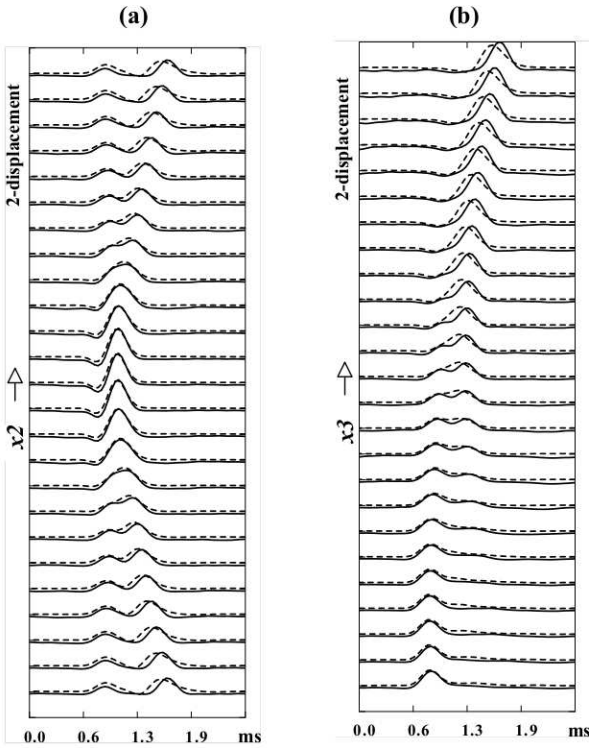

Figure 6

Figure 6. Comparison between the one–way equation result (dashed) and the 'exact' reference solution (solid) for pure halite. **(a)** x_2 section, x_3 midline ($ix3 = 25$), 2–component; **(b)** x_3 section, $ix3 = 30$, 2–component. In part (b) the profile/section is far enough from the acoustic axis that the slow qS2 wave can be seen to have a significant phase error (early).

profiles along x_2 (Figure 4(a)) show an asymmetry on either side of the acoustic axis (left column versus right column). The fast qS wave evidently contains most of the energy at left whereas the slow wave does so at right. In the middle column the energy is changing from the fast to the slow wave. These qualitative observations could be deduced by considering the qS2 polarization rotation in Figure 2.

In contrast, the sections along x_3 in Figure 4(b) show that the wavefront is 'torn' on either side of the acoustic axis (i.e. at large and small x_2, or the left and right columns). The offset between the fast and slow waves shown on either side of Figure 4 is probably unrealistically large (compared to the pulse width) for seismological data, but qualitatively this 'wavefront tearing' is a characteristic effect of an acoustic axis.

Figure 4(c) shows profiles of the weaker yet now nonzero 3–component, which we may term the 'anomalous' component. However, its importance relative to the larger 2–component is not revealed by this type of plot, and accordingly Figure 5 shows two–component seismograms along various x_2 and x_3 profiles. These show that the 3–component can grow from zero to become comparable with the initial 2–component, with a notable exception in part (a) along the mid–line $x_2 = 72$m (or index ix2=25, which lies in a symmetry plane for the pure–halite case). In fact, the 'gap' (or lacuna) in the 3–component along the x_2 section is another characteristic of the axial propagation. In this highly symmetric example, the 3–component shows waveforms which are perfectly antisymmetric about the central x_2 position, necessitating the zero central 3–component. However, we can expect to see such gaps more generally as they are associated with the eigen–polarization rotation (e.g. see also Figure 14(c) below). This zone of reduced 3–component is wider in x_2 sections lying just either side of the one depicted (i.e. away from the acoustic axis). Overall, note as well from Figures 4 and 5 that the waveforms on the main 2–component are quite distinct along profiles in the two orthogonal lateral (x_α) directions.

Evidently there are small ripples in the waveforms at the edges of the domain of propagation. There is the possibility that these are caused by incipient wavefront folding due to the concavity of the qS2 sheet, especially in directions away from the acoustic axis towards each of the three natural axes (there are mild 'ravines' in the slowness sheet along these directions, as can be seen Figure 1 of Rümpker & Thomson, 1994, for the qualitatively–similar case of cubic nickel). The waveform ripples may also be due to finite–difference inaccuracy at the edges, which can certainly arise when the grid spacing is made larger.

However, the waveforms in the central regions of Figures 4 and 5 can be regarded as accurate, and Figure 6 shows a comparison with the reference waveforms computed using separation of variables. Note, for example, the small negative swing in the central few traces of Figure

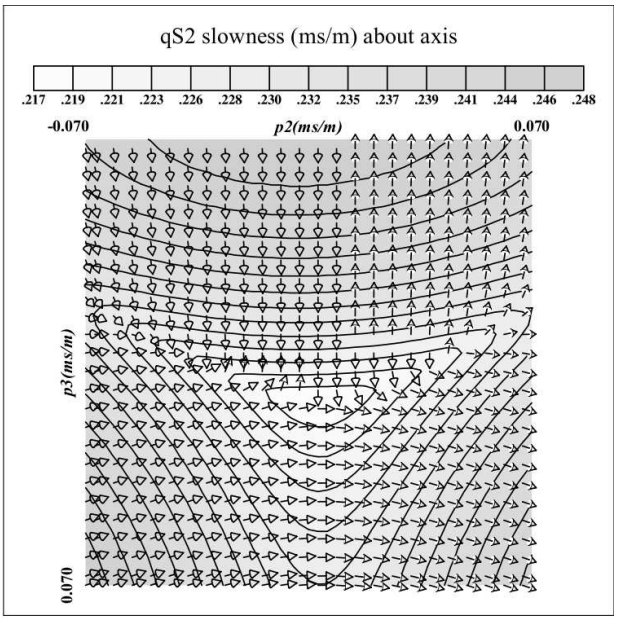

Figure 7

Figure 7. Contours of the 1–component of the qS2 slowness for pure quartz in the vicinity of the indentation shown in Figure 1(b). The rotated 1–axis and propagation direction are out of the page, at the centre of the plot. The 'free' polarization eigenvectors have been given arrowheads to emphasize the singularities which arise in any scheme which tries to define polarization continuously in this (p_2, p_3) tile. There appear to be three conical points (acoustic axes), where the polarizations form 'T' patterns and from which lines of singularity (polarization reversals) emanate.

6(a). Asymptotically, this swing is due to the Hilbert–transform effect of folded wavefronts, which is described somewhat more in the next section. Also noticeable in these central traces is a long–period variation (almost a negative d.c. shift) in the reference solution, which is due to the perimeter contributions to the two–dimensional slowness integrals. Taking this into account, the agreement between the one–way and reference solutions is very good in the central region. As the edges of the profile are approached, though, it is clear that the second–arriving qS wave from the one–way method is somewhat early (Figure 6(b)).

Pure halite is quite an extreme, if rather symmetric, case and yet it confirms the basic ideas of the vector one–way equation method. The phase errors in Figure 6, which have accumulated after propagating some 250 spatial pulse half–widths, are substantial and raise questions which can be addressed by considering an even more extreme case.

5.2 Pure Quartz – a pathological example

Pure quartz has even more dramatic slowness variations in the vicinity of the direction shown in Figure 1. There are in fact three closely–neighbouring acoustic axes (Figure 7). The propagator and its three–term Taylor series approximation are depicted in Figure 8, which indicates that even for this extreme material the quadratic approximation apparently does reasonably well. However, an important piece of the physics is made abundantly clear by this medium. Although the complicated polarization distribution does not in itself present a serious limitation for the 15° approximation, the severe indentation of the slowness surface and consequent wavefront folding place a definite limit on the propagation range over which this wave equation can be used.

In order to appreciate the qS2 wavefront folding which ensues, the Maslov phase is plotted in Figure 9 for a large propagation distance of 300m. For a receiver at the centre of the lateral grid (the origin), the Maslov phase is the 2–dimensional Legendre transformation w.r.t. x_α of the qS2 wavefront phase function (Kendall & Thomson, 1993). That is to say, it is the well–known function $\tau(p_\alpha)$ derived from tangent planes to $T(x_\alpha)$, the ray arrival–time function at the chosen range x_1 and for the given incident wave. Maxima and saddle points in Figure 9 indicate geometrical ray signals. We see that there should be three standard impulse arrivals corresponding to maxima, one somewhat later and at a larger p_3 value. There are also three almost–coincident Hilbert–transformed arrivals corresponding to intervening saddle points. These will actually be the earliest qS2 signals and will have a negative first motion.

At the initial data plane there is only the single stationary point (maximum) corresponding to the incident wave. As the range x_1 increases from zero the initial single maximum separates into the multiple stationary points, which migrate outwards to larger lateral slownesses. This outward migration corresponds to increasing importance for the developing wavefield of points on the initial wavefront which are close to the edges of the finite domain over which it was prescribed. The qS2 rays actually begin to cross immediately, causing wavefront folds to grow from vanishingly–small patches lying at the intersections of the acoustic axes with the initial–data plane. Eventually, at large x_1, the wavefield near the centre of the x_α plane depends on contributions associated with rays that emanate from the edges of the initial–data plane.

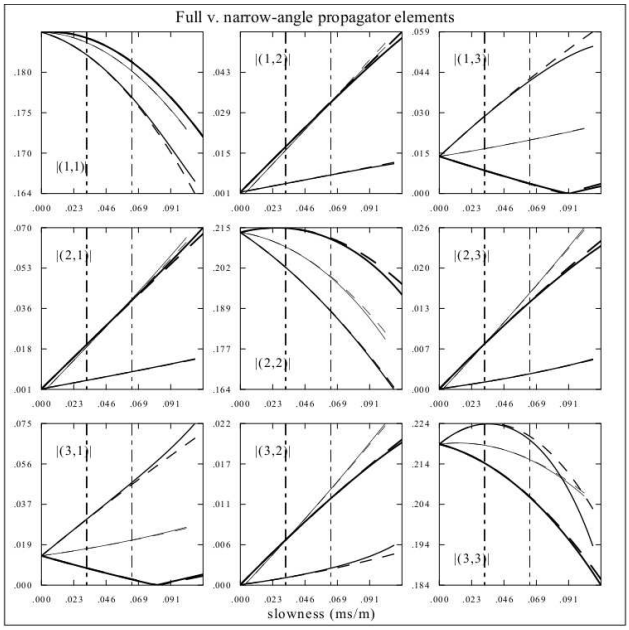

Figure 8

Figure 8. The nine elements of the exact propagator (solid lines) compared to those of the quadratic approximation (3.4) (dashed lines) in pure quartz, with lateral–slowness expansion point coinciding with the centre of the contour plot in Figure 7. Only the magnitudes are plotted, as indicated by the labels $|(1,1)|$, etc., for each frame. Each horizontal axis gives the magnitude of the lateral slowness 2–vector (p_2, p_3) or distance from the expansion point. Three azimuths have been selected, $10°$, $100°$ and $200°$, measured anticlockwise from the p_2–axis. These are signified by the three different lineweights. The two vertical centrelines depict the slownesses corresponding approximately to propagation at $8°$ and $15°$ to the 1–direction.

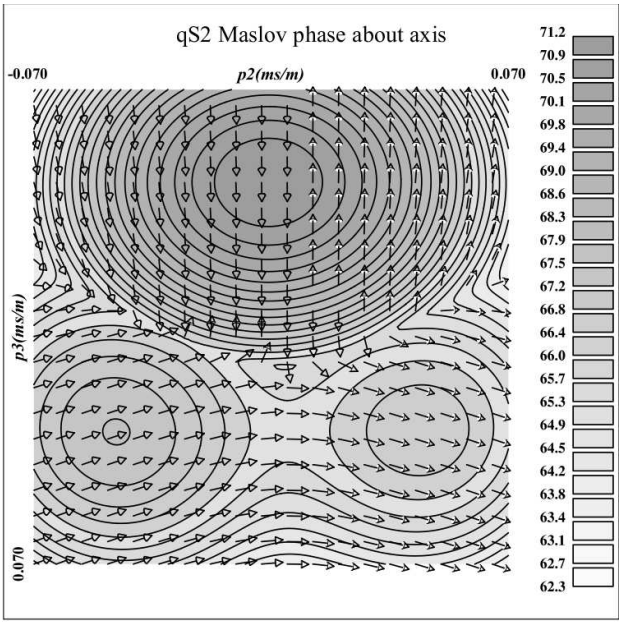

Figure 9

Figure 9. The qS2 Maslov phase corresponding to a receiver on the x_1 propagation axis at a range of 300m from the initial plane. See text for definition and discussion.

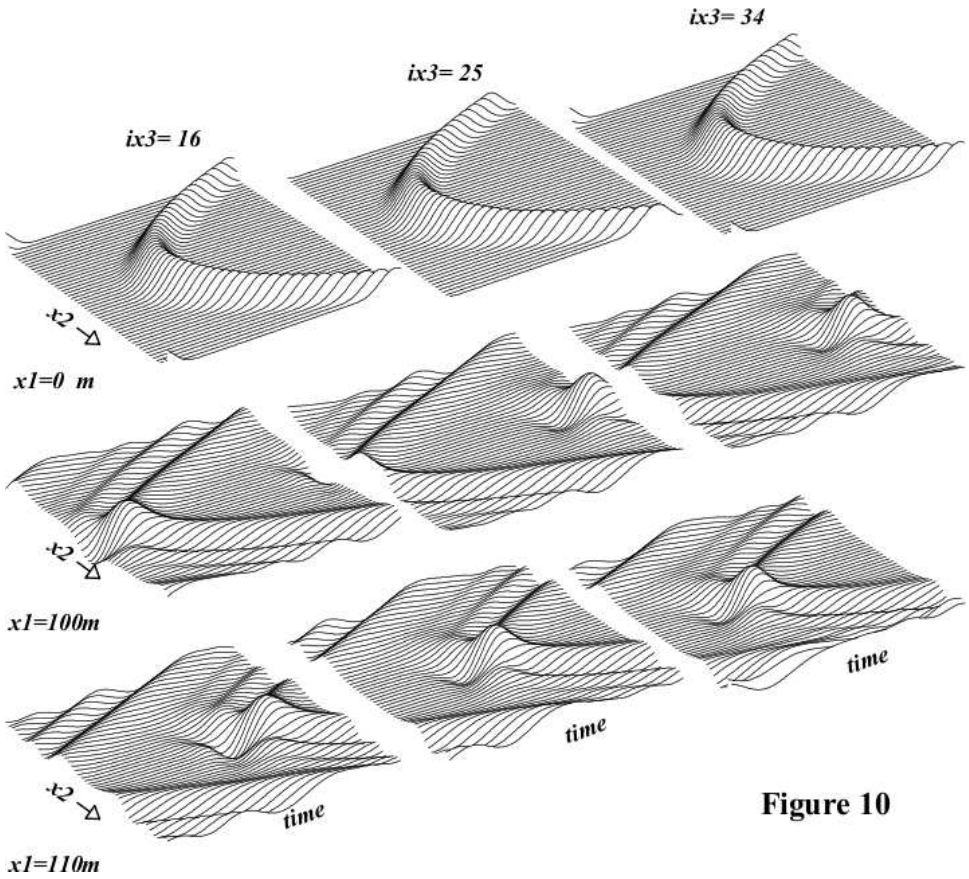

Figure 10. Waveforms of the 2–component in pure quartz at the initial x_1 plane and two penultimate planes (100m and 110m), plotted as profiles along the x_2 axis. The indices above the three columns signify the grid position of the profile in the x_3 direction. Since the grid is 49×49 points, index 25 represents a precise centre line, while positions 16 and 34 approximately bisect the intervals on either side. The first frame set reveals the curvature of the initial wavefront in comparison with the pulse width. The lower two frame sets indicate the movement of the wavefield in time after a 10m step along x_1. The wrap–around of the discrete time Fourier transform is apparent, but not a concern and again this must be considered reduce time. See text for discussion of the evolved waveforms, in particular the precursory depression seen in the centres of frames of the bottom row.

Thus our truncated initial–value problem and our approximate propagator have limitations to their well–posedness. One could introduce the idea of a Fresnel zone on the initial–data plane (by considering the widths of stationary points in Figure 9 for example). The radius of such a zone grows as x_1 increases, but it is important to recognize that there are several stationary–point contributions and that it is their combined effect which matters.

Taking guidance from Figure 9 we show waveforms which have propagated only 90m along x_1 (Figures 10 and 11). Once again only the central few traces can be considered accurate. Figure 10 shows quite clearly the enhanced amplitude and precursory negative swing (depression) for these central signals and in Figure 11 the reference solution verifies their general correctness. The precursory negative swing represents the emerging Hilbert–transformed folded qS2 wavefront. The reference–solution perimeter contributions are apparent in Figure 11, and include a somewhat–localised later–arriving pulse (see caption), which must be due to a perimeter (i.e. 1–dimensional) stationary–phase point. Towards the edges of the x_2 receiver line there are obvious phase errors signifying the limits of the 15° approximation (which predicts arrivals that are too early).

Overall, the one–way equation results are as one might expect and from this very extreme example we conclude that for short paths (under 30 spatial pulse half–widths in this case) the 15° approximation may still have some utility. However, a more widely–applicable method, such as the phase–screen approach, would clearly be better. These intuitively–expected conclusions could be supported by mathematical analysis of the rays or characteristics of the 15° equation, in addition to the numerical examples. Interestingly, if this one–way equation is used over a somewhat longer propagation distance, say 135m, it does appear to create a first–arriving wavefield apparently riding on a folded wavefront, but the waveforms are not accurate. Caution must therefore be exercised and ray tracing can be used to define the domain of applicability, via the Maslov phase, if there is doubt. Space does not permit us to show the exact/reference waveforms for the many distinct multiple arrivals that exist at longer ranges or higher frequencies, but qualitatively similar signals have been presented by Rümpker & Thomson (1994) in the very–high frequency range.

These observations apply as well to the previous pure halite example, where at 200m an incipient Hilbert–transformed precursor could be perceived and hence the angular spectrum on the initial plane may have been been only just sufficient for the range considered. There

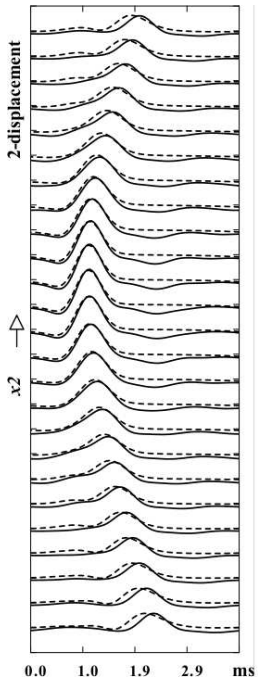

Figure 11

Figure 11. Comparison between the one–way equation result (dashed) and the 'exact' reference solution (solid) for pure quartz. This is an x_2 section at the x_3 midline. Note the weak negative pulse between 1.9 and 2.9ms, which is a perimeter (1–D) stationary–point signal. See text for further discussion.

were also qS2 phase errors (Figure 6) indicating the same basic problem, namely that the 15° has a definite range limitation when slowness surface indentations are important.

5.3 Three more–moderate polycrystal examples

In more moderate, and prevalent, cases the applicability of the 15° is far less restricted and the main effect of acoustic axes on gently–curved wavefronts will be subtle waveform changes as described in the introduction. The three polycrystal examples of Figure 1(c–e) are taken to be representative and they are grouped together as we wish to emphasize the more–or–less generic effect of conical points on waveforms in this regime. Differences in initial conditions (ratio of qS1 to qS2) can alter the waveforms significantly, of course, but in cases where they are comparable results such as Figure 12(a–c) are obtained. In each case we see two roughly–equal qS signals that merge as an acoustic axis is approached. In the sheared halite (Figure 12(a)) the pulse properties are as above for pure halite and the path length is about 250 pulse half–widths. For the mylonite model (Figure 12(b)) the pulse half–width is about 0.4ms in time and about (0.4ms)/(0.24ms/m)=1.7m in space. Thus the total path is (200m)/(1.7m) $\approx$ 120 spatial pulse half–widths in this model.

Figure 13 shows a comparison between the 15° equation results and those of the exact reference solution in the sheared-halite model. The agreement is very good, especially after propagating so many pulse widths. The results of Figure 13(b) are particularly encouraging, where the weaker, anomalous 3–component of the waveforms is compared between the two techniques. We conclude from Figure 13 that sufficient accuracy can indeed be obtained for practical applications in which, roughly speaking, the waveforms will be low–pass filtered versions of those shown. It is actually gratifying that the numerical computations can be carried out in of order ten minutes even for the more extreme parameter ranges used here.

The same spatial dimensions have actually been used for the ridge–LPO elasticity results of Figure 12(c), to emphasize the generic properties. Here the temporal pulse half–width is 0.3ms and the spatial pulse half–width at the same frequencies is about 1.4m, as the wavespeed is somewhat higher than, say, for halite. Thus the 200m path length is about 70 pulse half–widths. Scaling down to lower frequencies we can estimate that for a signal of width 0.1s (i.e. circa 10Hz) a path length around 70km would generate similar waveforms. A pulse ten or more times wider (period $>$ 1s) would be more realistic for a seismic wave used to probe the upper mantle, and applying a corresponding filter to the waveforms of Figure 12(c) suggests that the signal variations will then indeed be subtle. However, it should be recalled that the shear–wave splitting is increasing away from the axis and the stronger splitting would certainly be visible for this particular elasticity at those lower frequencies for a 70km path.

To support this, the example of Figure 14 shows waveforms computed in the ocean–ridge elasticity for spatial dimensions and frequencies closer to upper–mantle signals. Here the lateral grid size is 240km by 240km, with grid spacing 5km. The propagation path length is 100km and the pulse half–widths are about 0.25s in time and 1.2km in space. Thus the propagation path is approximately 80 spatial pulse half–widths. While the dominant frequency of 4Hz is still somewhat higher than would be available in the data, it should again be borne in

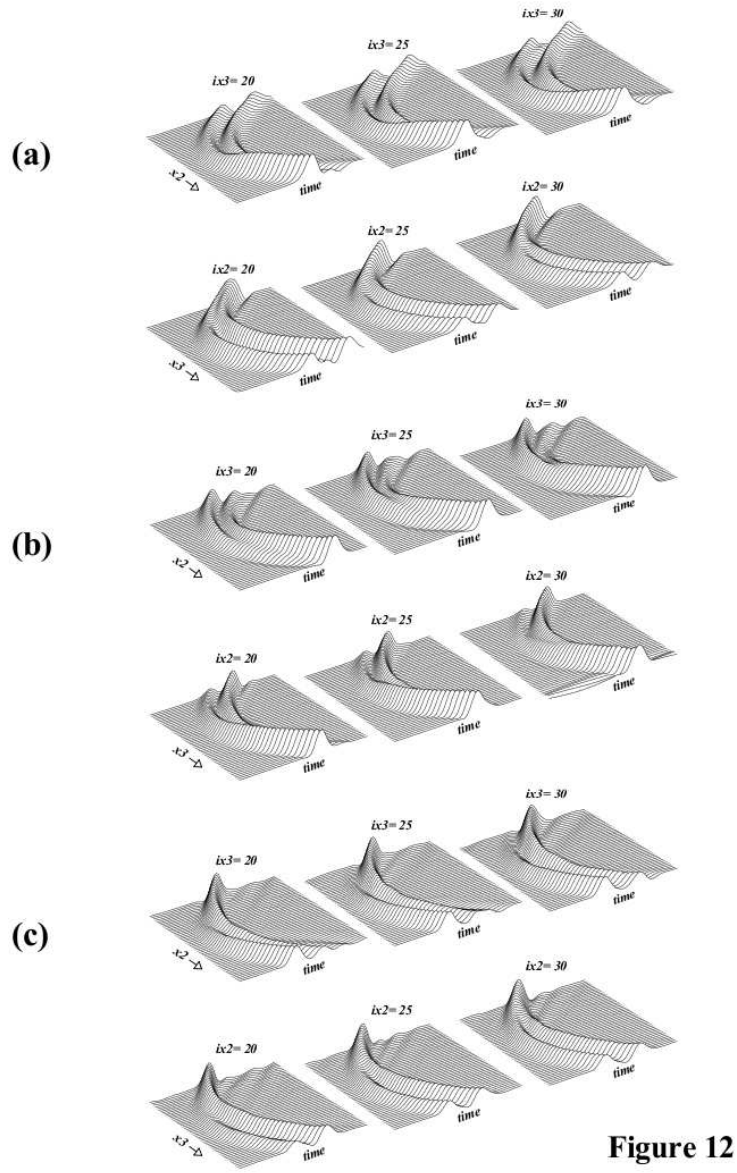

Figure 12

Figure 12. The highly–comparable waveforms of the 2–component along x_2 and x_3 sections after propagating to $x_1 = 200$m subparallel to acoustic axes in the three moderately–anisotropic polycrystal elasticities of **(a)** sheared halite; **(b)** quartz–rich mylonite; **(c)** the olivine LPO mantle texture model. The three columns indicate different choices for the remaining third dimension (x_3 or x_2, by grid index). See text for discussion.

mind that we are modelling a domain of moderate splitting approaching an acoustic axis. Visual inspection of Figure 14(a) suggests quite clearly that for signals around 2Hz the effects of conical points will be to effectively double (or halve) the apparent pulse widths along some transects. Similarly, Figure 14(b) shows how the splitting on the anomalous or initially–unexcited component (again the 3–component in this case) can cause significant signals with a characteristic bipolar waveform.

Lastly, Figure 14(c) shows an x_3 section for a slightly different path near the acoustic axis. This example has the previously–seen gap/polarity–change in the anomalous 3–component that can arise as a result of the polarization rotations. It also shows broadening of the main 2–component signals at lower x_3 positions, and it is important to note that there is an offset along x_3 between the gap and the broadened pulses. This offset is intuitively in keeping with the polarization rotations around the axis and the separation of the slowness sheets on moving away, and this example serves to remind us that the characteristics of a single anisotropic feature (i.e. the axis) may appear on distinct seismograms. Thus it is important to study the vector waveform evolution along the entire profile.

While these homogeneous–medium examples adequately demonstrate the possibilites for mantle paths and periods such as these, in

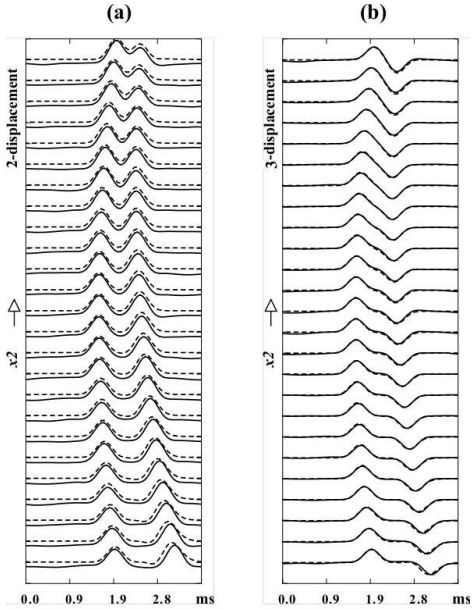

Figure 13

Figure 13. Comparison of the displacement waveforms obtained after 200m of propagation using the 15° one–way equation (dashed) and the 'exact' reference solution (solid) in the sheared–halite model. **(a)** 2–component, **(b)** 3–component. Slowness integration perimeter contributions to the reference solution are most apparent as a roughly d.c. shift in part (a). See text for discussion.

complex structures such as that depicted in Figure 4 of Blackman et al. (1996) the effects of wavetype coupling and smoothing by medium inhomogeneity are expected to be important. This will be the topic of future papers (Angus & Thomson, in prep.).

6 DISCUSSION

The relationship between waveforms and underlying elasticity soon becomes complicated when wavefronts are curved and the integrated effect of a plane–wave spectrum needs to be considered. However, despite the numerous polarization, path–length and frequency scenarios, an intuitive understanding should be obtainable with the aid of a modest amount of waveform modelling.

We have presented a method for simulating waveforms in anisotropic and inhomogeneous media which balances computational speed and the necessary physical content. Although the limitations of the theory are evident and the examples presented are deliberately not too complicated, we believe the method has clear potential. The particular form of one–way equation implemented here is part of a hierarchy of approximations which should encompass a wide range of practical cases.

The method is capable of incorporating the effects of smooth variations in the medium across the wavefront, since the propagator in (2.3) and coefficient matrices in (3.8) depend on the lateral coordinate x_α. Such variations may be on the scale of a Fresnel zone or less, so long as the notion of a primary wave with a dominant propagation direction is still appropriate. The challenge of using this knowledge with data to constrain Earth structure remains a serious one and it is for this reason that we consider the local nature and computational efficiency of the method to be important.

The reader may be wondering how density variations appear in the theory, and in fact the answer is they arise at the next order in $1/\omega$ in the asymptotic expansion that yields the factorized wave equation. This is in keeping with the way in which density terms arise in the standard ray method. Although it is not too difficult to incorporate such higher terms, the leading terms emphasize the controlling influence of the vector polarizations and differential phase speeds, and these terms ought to be sufficient in many cases.

Another fundamental point is that fine–scale features such as conical points can be either smoothed away or made dramatically apparent, as key parameters vary. Effects such as shear–wavefront tearing, enhanced or diminishing amplitudes, anomalous components, and pulse broadening may all arise. With high–frequency pulses these effects can be seen using a relatively low value of incident wavefront curvature, or equivalently a single distant source. As frequency–content decreases, though, a wider range or spectrum of incident wave slowness may be required, either from a single nearby source or a range of distant source positions. The Cartesian implementation of the 15° approximation may not be adequate in the former scenario, so that a curvilinear coordinate version may be required or even a more complete representation based on equation (2.3) (e.g. a phase–screen limit).

Although the 15° approximation is the most restrictive, it does indicate how the elasticity–tensor and slowness–surface local directional properties influence the waves, namely via the Taylor expansion (3.4). This presumably has implications for interpretation and the 'auto-

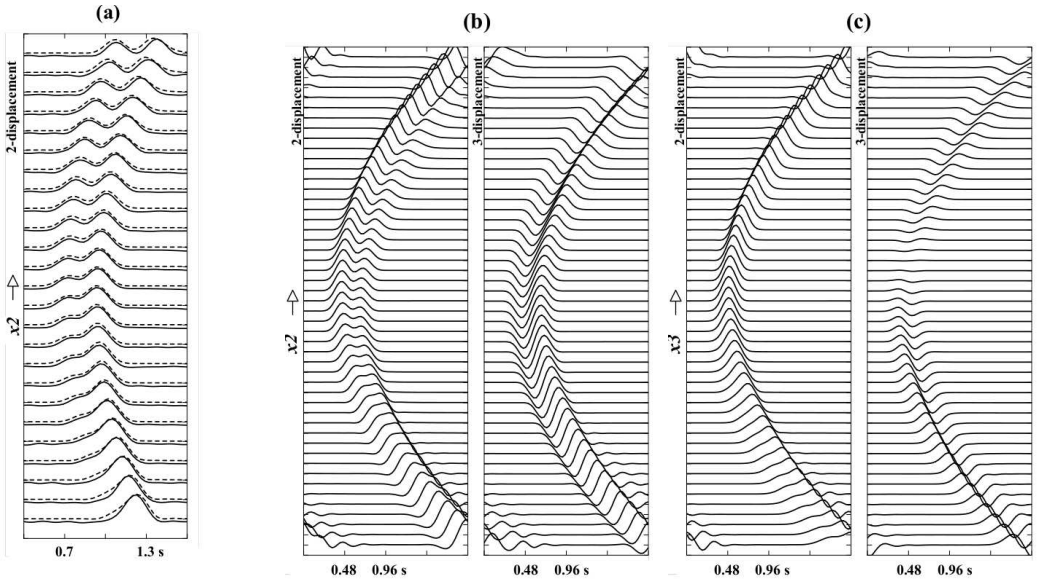

Figure 14. Comparison of the 2–displacement waveforms obtained after 100km of propagation using the one–way equation (dashed) and the reference solution (solid) in the olivine LPO model, at lower frequencies and with a (49×49 point) lateral–grid spacing of 5km. The initial wavefront again spans an angular range of $\pm 15^\circ$ over the enlarged 240km$\times$240km area. This plot verifies that the numerical method can be scaled appropriately and that the Cartesian coordinates are likely to be sufficiently accurate for many cases of interest. **(b)** The 2– and 3–components compared. The former displays siginificant waveform differences at large and small x_2, since the acoustic axis is neared somewhere in the middle. The latter is initially zero and has grown by splitting into qS1 and qS2 waves with opposing polarities (creating a bipolar net waveform). **(c)** An x_3 section near the same axis, showing a gap/lacuna in the 'anomalous' 3–component, the position of which is somewhat offset from the receivers showing pulse–broadened 2–components at lower x_3 positions. See text for further discussion.

mated' inversion of waveform data. In a pioneering study Haddon & Husebye (1978) analysed apparently–systematic teleseismic amplitude variations across the NORSAR array using their own one–way propagator. The 'focussing' which they sought to explain could now conceivably be augmented by polarization and entire waveform information (including shear–wave splitting). The theoretical details and the inherent non–uniqueness of such teleseismic waveform inversion have yet to be clarified, but a key step is the ability to model gradual vector waveform evolution across a dense array of receivers. With such data the prospects are good for enhanced anisotropy studies exploiting the polarization variations such as those of Figure 1.

ACKNOWLEDGMENTS

Doug Angus gratefully acknowledges Dave Lyness and Bullard Laboratories, Cambridge University, for providing access to their computer systems during the initial stages of this Ph.D. project. Mike Kendall and Geoff Lloyd are thanked for providing the elastic parameters used, and G. Lloyd & S. Valcke are thanked for discussing their petrofabric analyis. This work was supported by a grant from Imperial Oil (Canada) and NSERC Individual Research grants to the second two authors. D. Angus was also supported by scholarships from the Canadian Society of Exploration Geophysicists and Queen's University.

REFERENCES

Al'shits, V. I. & Lothe, J., 1979, Elastic waves in triclinic crystals. I. General theory and the degeneracy problem, *Sov. Phys. Crystallogr.*, **24**, 387–392.

Bakulin, A., Grechka, V. & Tsvankin, I., 2000, Estimation of fracture parameters from reflection seismic data: Part III: Fractured models with monoclinic symmetry, *Geophysics*, , **65**, 1818–1830.

Blackman, D. K., Kendall, J–M., Dawson, P. R., Wenk, H.–R., Boyce, D. & Morgan, J. P., 1996, Teleseismic imaging of subaxial flow at mid–ocean ridges: traveltime effects of anisotropic mineral texture in the mantle, *Geophys. J. Int.*, , **127**, 415–426.

Bostock, M. G., 1997, Anisotropic upper–mantle stratigraphy and architecture of the Slave craton, *Nature*, **390**, 392–395.

Červený, V., 2001, *Seismic ray theory*, Cambridge Univ. Press, London.

Chapman, C. H. & Shearer, P. M., 1989, Ray tracing in azimuthally anisotropic media — II. Quasi–shear wave coupling, *Geophys. J.*, **96**, 65–83.

Christie, M., MacBeth, C. & Subbey, S., 2002, Multiple history–matched models for Teal South, *Leading Edge*, **21(3)**, 286–289.

Claerbout, J. F., 1976, *Fundamentals of geophysical data processing*, Blackwell Scientific Publications, Oxford.

Crampin, S. & Yedlin, M., 1981, Shear–wave singularities of wave propagation in anisotropic media, *J. Geophys.*, **49**, 43–46.

Fornberg, B., 1996, *A practical guide to pseudospectral methods*, Cambridge University Press, Cambridge, U.K.

Frazer, L. N. & Gettrust, J. F., 1984, On a generalization of Filon's method and the computation of the oscillatory integrals of seismology, *Geophys. J. R. astr. Soc.*, , **76**, 461–481.

Guest, W. S., Thomson, C. J., & Spencer, C. P., 1993., Anisotropic reflection and transmission calculations with application to a crustal seismic survey from the East Greenland shelf, *J. geophys. Res.*, , **98**, 14161–14184.

Haddon, R. A. W. & Husebye, E. S., 1978 Joint interpretation of P–wave time and amplitude anomalies in terms of lithospheric heterogeneities, *Geophys. J. R. astr. Soc.*, , **55**, 19–43.

Helffrich, G., Wiens, D. A., Vera, E., Barrientos, S., Shore, P., Robertson, S. & Adaros, R., 2002, A teleseismic shear–wave splitting study to investigate mantle flow around South America and implications for plate–driving forces, *Geophys. J. Int.*, , **149**, F1–F7.

Herwanger, J. V., Worthington, M.H., Lubbe, R., Binley, A. & Khazanehdari, J., 2003, A comparison of crosshole electrical and seismic data in fractured rock, submitted to *Geophysical Prospecting*, September 2001.

Kay, I., Sol, S., Kendall, J-M., Thomson, C. J., White, D., Asudeh, I., Roberts, B. & Francis, D., 1999, Shear wave splitting observations in the Archean Craton of Western Superior, *Geophys. Res. Lett.*, , **26**, 2669–2672.

Kendall, J-M. & Thomson, C. J., 1993, Maslov ray summation, pseudocaustics, Lagrangian equivalence and transient seismic waveforms, *Geophys. J. Int.*, **113**, 186–214.

Kendall, J–M., Sol, S., Thomson, C. J., White, D. E., Asudeh, I., Snell, C. S. & Sutherland, F. H., 2002, Seismic heterogeneity and anisotropy in the Western Superior Province, Canada: Insights into the evolution of an Archaean craton, in Fowler, C. M. R. et al. (eds.) *The Early Earth: Physical, Chemical and Biological Development*, Geological Society, London, Special Publications, 199.

Komatitisch, D. & Tromp, J., 1999, Introduction to the spectral element method for 3–D seismic wave propagation, *Geophys. J. Int.*, **139**, 806–822.

Kravtsov, Yu. A. & Orlov, Yu. I., 1990, *Geometrical optics of inhomogeneous media*, Springer–Verlag, Berlin.

Le Rousseau, J. H. & de Hoop, M. V., 2001, Scalar generalized–screen algorithms in transversely isotropic media with a vertical symmetry axis, *Geophysics*, **66**, 1538–1550.

Lloyd, G. & Kendall, J-M., 2003 Petrofabric derived seismic properties of a mylonitic quartz simple shear zone; implications for seismic reflection profiling, in Geol. Soc. London Sp. Publ. *Petrophysical Properties of Crystalline Rocks*, eds. P. Harvey, T. Brewer, P. Pezard & V. Petrov.

Mainprice, D. & Silver, P. G., 1993, Interpretation of SKS–waves using samples from the subcrustal lithosphere, *Phys. Earth planet. Inter.*, , **78**, 257–280.

Martin, B. E. & Thomson, C. J., 1997, Modelling surface waves in anisotropic structures, *Phys. Earth planet. Inter.*, , **103**, 253–279.

Musgrave, M. J. P., 1972, *Crystal Acoustics*, Holden–Day, San Francisco.

Raymer, D. G., Tommasi, A. & Kendall, J–M., 2000, Predicting the seismic implications of salt anisotropy using numerical simulations of halite deformation, *Geophysics*, , **65**, 1272–1280.

Rümpker, G. & Thomson, C. J., 1994, Seismic–waveform effects of conical points in gradually varying anisotropic media, *Geophys. J. Int.*. **118**, 759–780.

Rümpker, G. & Kendall, J–M., 2002, A Maslov–propagator seismogram for weakly anisotropic media, *Geophys. J. Int.*, **150**, 23–36.

Tannehill, J. C., Anderson, D. A. & Pletcher, R. H., 1997, *Computational fluid mechanics and heat transfer*, Taylor & Francis, Washington, D.C.

Thomson, C. J., 1999. The 'gap' between seismic ray theory and 'full' wavefield extrapolation, *Geophys. J. Int.*, **137**, 364–380.

Vavry'v cuk, V., 1999, Applicability of higher–order ray theory for S wave propagation in inhomogeneous weakly anisotropic elastic media, *J. Geophys. Res.*, **104**, 28829–28840.

Weiss, T., Siegesmund, S., Rabbel, W., Bohlen, T. & Pohl, M., 1999, Seismic velocities and anisotropy of the lower continental crust: A review, *Pure appl. geophys.*, **156**, 97–122.

Winterstein, D. F., & De, G. S., 2001, VTI documented, *Geophysics*, **66**, 237–245.

Woodhouse, J. H., 1974, Surface waves in a laterally varying layered structure, *Geophys. J. R. astr. Soc.*, **37**, 461–490.

Wu, R.-S., 1994, Wide–angle elastic wave one–way propagation in heterogeneous media and an elastic–wave complex screen method, *J. geophys. Res.*, **99**, 751–766.